



PAPER • OPEN ACCESS

Monte Carlo simulation of ultrafast nonequilibrium spin and charge transport in iron

To cite this article: J Briones *et al* 2022 *J. Phys. Commun.* **6** 035001

View the [article online](#) for updates and enhancements.

You may also like

- [Modelling ultrafast laser ablation](#)
Baerbel Rethfeld, Dmitriy S Ivanov, Martin E Garcia et al.
- [Time-resolved electron kinetics in swift heavy ion irradiated solids](#)
N A Medvedev, R A Rymzhanov and A E Volkov
- [Ultrafast electron-lattice thermalization in copper and other noble metal nanoparticles](#)
Denis Mongin, Paolo Maioli, Julien Burgin et al.



PAPER

Monte Carlo simulation of ultrafast nonequilibrium spin and charge transport in iron

OPEN ACCESS

RECEIVED

2 December 2021

REVISED


22 February 2022

ACCEPTED FOR PUBLICATION

24 February 2022

PUBLISHED

7 March 2022

J Briones , H C Schneider and B Rethfeld

Department of Physics and OPTIMAS Research Center, TU Kaiserslautern, Erwin Schroedinger Str. 46, 67663 Kaiserslautern, Germany

E-mail: briones@physik.uni-kl.de

Keywords: spin, transport, monte carlo, nonequilibrium

Original content from this work may be used under the terms of the [Creative Commons Attribution 4.0 licence](https://creativecommons.org/licenses/by/4.0/).

Any further distribution of this work must maintain attribution to the author(s) and the title of the work, journal citation and DOI.

**Abstract**

Spin transport and spin dynamics after femtosecond laser pulse irradiation of iron (Fe) are studied using a kinetic Monte Carlo model. This model simulates spin dependent dynamics by taking into account two interaction processes during nonequilibrium: elastic electron–lattice scattering, where only the direction of the excited electrons changes, and inelastic electron–electron scattering processes, where secondary electrons are generated. An analysis of the spin dependent particle kinetics inside the material shows that a smaller elastic scattering time leads to a larger spatial spread of electrons in the material, whereas generation of secondary electrons extends the time span for superdiffusive transport and increases the spin current density.

1. Introduction

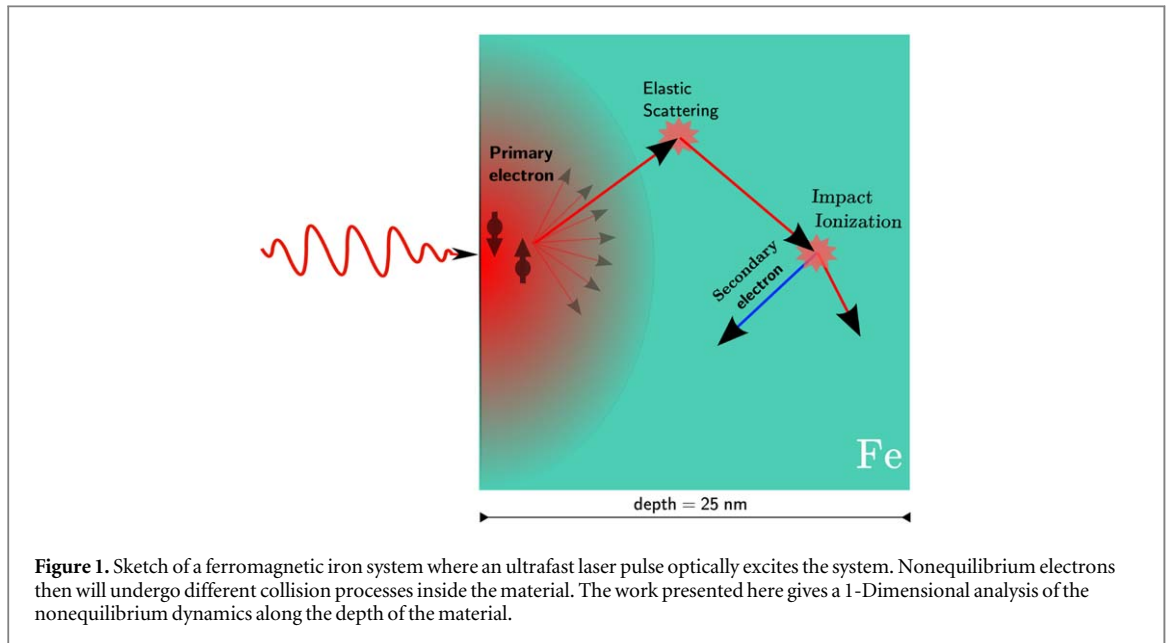
Following the discovery of ultrafast demagnetization in metallic ferromagnets and its connection to hot electron spin transport, the interplay of optical excitation, magnetization dynamics and transport has been under active investigation. During and after the optical excitation of ferromagnets, the electronic system is driven out of equilibrium, and later thermalizes via different processes [1–5].

The dynamics of spin transport were first studied by Battiato *et al* [6] identifying an intermediate regime of the spin transport, labeled as superdiffusive transport. The contribution to demagnetization dynamics was later supported by experiments [7, 8]. Another recent study of this effect introduced a particle in cell simulation [9] to solve the Boltzmann equation for spin dependent hot-electron transport.

In order to understand the influence of the different scattering interactions in spin transport we analyze the spatio-temporal dynamics by tracing spin and charge in dependence of depth by considering free electron states for energies above the Fermi energy. We propose for this type of system an application of the kinetic Monte Carlo technique. Figure 1 shows a sketch of a trajectory of an excited electron undergoing several collision processes. Within the applied Monte Carlo method such trajectories are traced and statistically evaluated.

Monte Carlo simulations have been widely used in studies of hot carriers dynamics, such as radiation biology [10–12], nuclear physics [13] and particle transport [14] among many others. In this paper we present a Monte Carlo approach and its capabilities in analyzing the influence of secondary electrons generation in spin dynamics and spin transport.

The outline of the paper is as follows: we will first present a model of excitation process, thereby briefly introduce how the kinetic Monte Carlo technique works. We explain how an electron is treated during laser excitation and discuss the role of the spin dependent density of states. The next section will focus on the possible scattering processes that are taken into account in our simulation. Finally we present the results in depth-dependence for different scattering times in ferromagnetic iron after ultrafast laser excitation with 6 eV photon energy, as well as some results showing the influence of secondary electrons generation in the particle kinetics.



2. Excitation process

In this section we discuss the algorithm used for the simulations applied in this paper, and present an analysis of the energy density of excited electrons when only photoexcitation is considered.

2.1. Monte Carlo algorithm

The asymptotic Monte Carlo trajectory method [15] is a statistical technique that models binary collision interactions by random sampling a very large number of trajectories until a result converges. The algorithm used for random sampling of a variable x is done using probability theory. In probability theory one integrates the probabilities of all possible events $p(x)$, where $x_{\min} \leq x \leq x_{\max}$, into a variable called cumulative distribution function (CDF) $F(x)$ [16]. One can map the CDF onto the range of random variables R , where $R \in [0, 1]$ and R is distributed uniformly:

$$R = \frac{F(x) - F(x_{\min})}{F(x_{\max}) - F(x_{\min})} = \frac{\int_{x_{\min}}^x p(x) dx}{\int_{x_{\min}}^{x_{\max}} p(x) dx}, \quad (1)$$

The variable x is then uniquely determined in dependence on R . Now we use this general idea to perform random-sampling of any required variable for the different types of interactions.

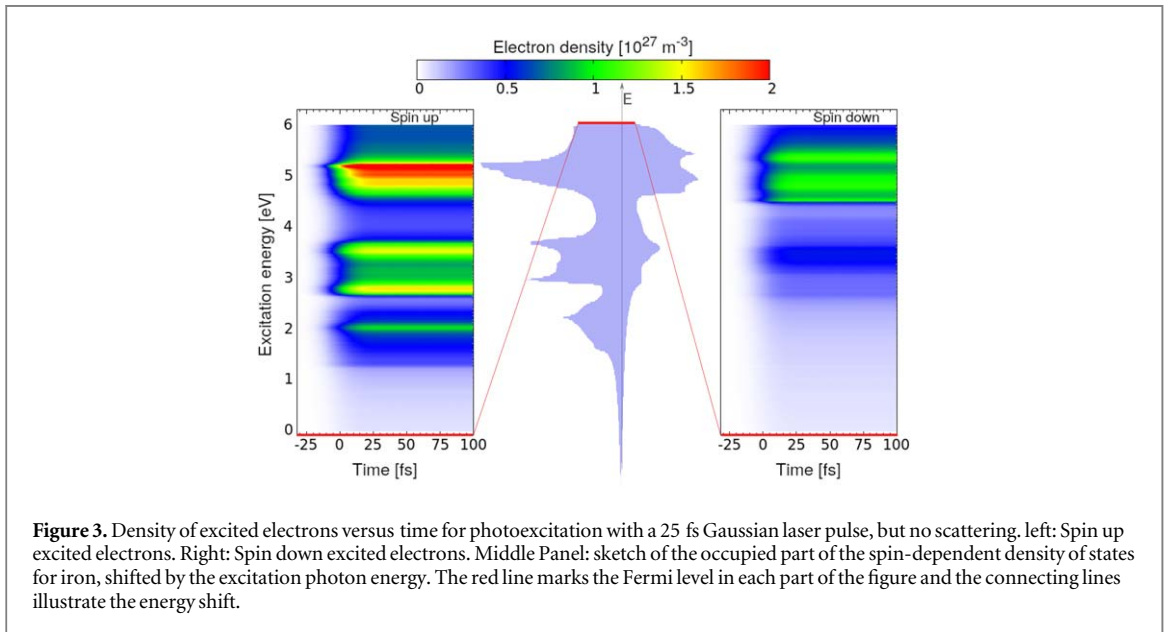
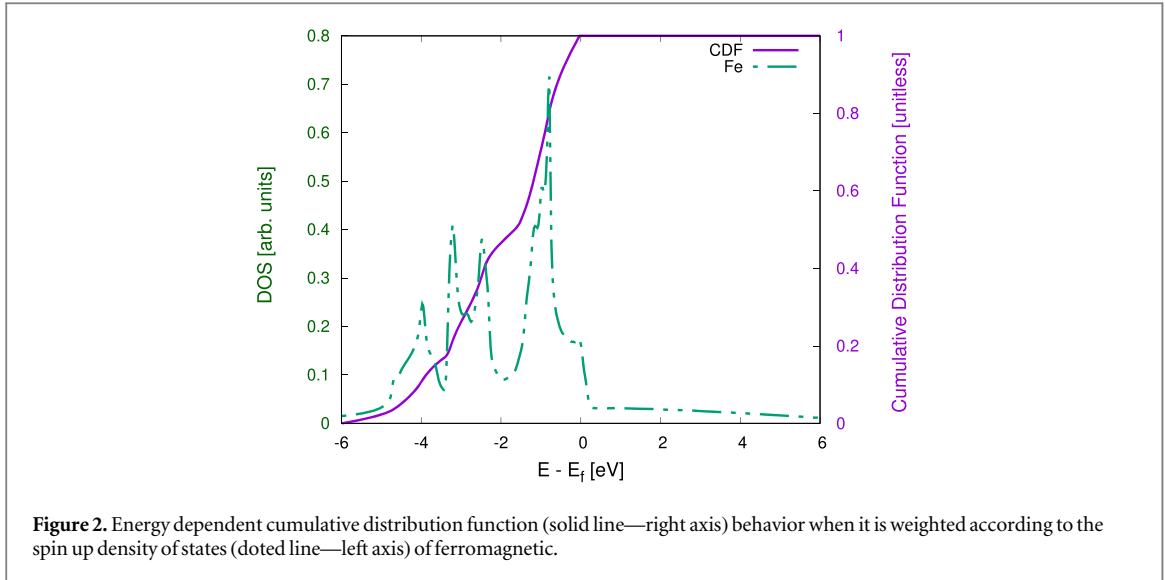
Random sampling is also used to decide whether certain interaction or excitation processes happen. In these cases we make use of the discrete form of equation (1). Examples of random sampling are shown in figures 2 and 4 for the excitation of electrons. The treatment of interactions in this simulation is discussed in section 3 of this work.

2.2. Laser and material parameters

We simulate the excitation of a ferromagnetic iron (Fe) layer with a 25 nm depth with a temporally Gaussian laser pulse with full width half maximum (FWHM) of 25 fs and 6 eV photon energy. The simulation works for any spin dependent density of states. Here, we take the data for iron from [17].

The excitation of an electron from an occupied band is modeled by choosing for equation (1) a probability of excitation according to the material's density of states below E_F . Figure 2 shows the calculated energy dependent cumulative distribution function (solid line) for the density of states for spin up electrons (dash-dotted line). States above E_F , will be considered as free electron states with a constant effective mass.

As a first test we study only photoexcitation, without any scattering processes for the excited electrons. Figure 3 shows the color-coded electron density of excited spin up (or majority) and spin down (or minority) electrons after photoexcitation in dependence on time and kinetic energy above E_F . The laser pulse with 25 fs duration is centered around $t = 0$. The results show that a larger density of electrons is excited from $3d^{\uparrow}$ states in comparison to the $3d^{\downarrow}$, i.e., predominantly majority electrons are excited. The spin-dependent density of states, which is sketched in the background of figure 3, shows that the excited energy-resolved electron density reflects the spin dependent density of states of the occupied bands in ferromagnetic iron.



3. Different scattering processes

We trace the dynamics of particles after laser excitation by pure jump processes [12, 18, 19]. In our approach, we consider free electron states above E_F as essentially free and focus on the influence of high energy electrons in spin transport. During the simulation any electron interaction process is treated by random sampling. For the excitation process already discussed above, the initial direction of the excited electrons will be taken as random direction.

We consider the probability that an electron has not suffered any collision between $\tilde{t} = 0$ and t as

$$p(t) = \exp \left[- \int_0^t \nu(E(\tilde{t})) d\tilde{t} \right]. \quad (2)$$

Here, ν is the total scattering rate defined as the sum of all possible scattering transitions. It is dependent on the energy E of the considered electrons, which may vary in time. In fact, this equation should be solved for each scattering event. However, we simplify the calculation as proposed in [20] by assuming a constant scattering rate ν_0 . Then, the time of free flight τ can be sampled with the random variable $R \in [0, 1]$ as

$$\tau = -\nu_0^{-1} \log(R). \quad (3)$$

However, assuming a constant total scattering rate, independent of energy, is a statistical overestimation. To compensate, we introduce a further ‘collision’ with an energy-dependent probability, which allows the particle to continue its trajectory unperturbed.

We randomly sample which collision takes place by using the individual collision frequencies and form the cumulative distribution function in order to solve equation (1). We take two interactions into account, namely the electron–nucleus interaction, considered here as an elastic scattering process, and the electron–electron impact ionization, where energy is transferred in an inelastic process to a secondary electron. In the following subsections we analyze these interactions in detail and provide the equations or parameters used.

3.1. Elastic scattering: electron–nucleus interaction

High-energy electrons are scattered nearly elastically by nuclei, i.e., they change their direction of motion. Here, we parametrize this interaction by two important quantities: the angle of deflection (θ) and the elastic scattering rate (τ_{el}^{-1}). We will follow a procedure which has been applied to different materials, see [21–23]. In order to obtain the angle of deflection θ for solving equation (1) we choose as probability function the differential cross section ($\frac{d\sigma}{d\Omega}$), described here by the Mott cross section [24]:

$$\frac{d\sigma}{d\Omega} = |f(\theta)|^2 + |g(\theta)|^2, \quad (4)$$

where θ is the scattering angle, $f(\theta)$ and $g(\theta)$ are the scattering amplitudes which can be obtained from the following expressions:

$$f(\theta) = \frac{1}{2iK} \sum_{l=0}^{\infty} \{(l+1)[e^{2i\delta_l} - 1] + l[e^{2i\delta_{l-1}} - 1]\} P_l(\cos \theta), \quad (5)$$

$$g(\theta) = \frac{1}{2iK} \sum_{l=1}^{\infty} \{(l+1)[-e^{2i\delta_l} + e^{2i\delta_{l-1}}]\} P_l^1(\cos \theta). \quad (6)$$

Here, $K^2 = W^2 - 1$, where W is the total energy of the incident electron in atomic units, δ_l is the phase shift for the l -th partial wave and P_l and P_l^1 are the ordinary and associated Legendre Polynomials, respectively.

We have now a set of equations that will allow us to obtain values of the angle of deflection by using equation (1). The next step is to obtain an expression for the elastic scattering rate. In principle, it can be deduced from the total scattering cross section, accessible by the integration of equation (4), together with the density of collision partners. It depends on energy, material and temperature [25–28]. In our kinetic MC approach we have no access to heat flow and energy relaxation between the subsystems. Here, we focus on momentum changes and the net effect of the scattering between electrons and nuclei by assuming a constant characteristic time τ_{el} . We will analyse the dynamics for two values: $\tau_{el} = 25$ fs taken from [29], which was used to study spin transport and spin dynamics in [9, 30], and $\tau_{el} = 12$ fs from [31, 32]. We will not take into account the loss of energy due to recoil for this simulation but focus solely on the change of the direction of flight.

3.2. Inelastic scattering: impact ionization

When a high-energy electron interacts with electrons below and close to E_F in the occupied band and generates secondary electrons (SE), we will regard this as an inelastic collision. A high-energy primary electron with energy E can lose the energy ΔE to a second electron, thereby ionizing the latter. The SE produced in this process can ionize further secondary electrons in a cascade process. The generation of SE by cascade process is believed to have an important influence on ultrafast spin transport [33]. The process of secondary electrons generation has been studied in different materials, going back to [34, 35].

Our numerical treatment of the SE generation process is as follows. In order to select the newly excited electron we follow the same procedure as explained in section 2.2, where the probability of excitation depends on the material's density of states, with the constraint that two particles cannot be in the same state and thus we avoid selecting two electrons from the same occupied state twice. We distinguish the spin of the newly excited electrons by selecting them from the spin-resolved density of states and weight the probabilities accordingly.

The energy lost by the primary electron ΔE is used to ionize a secondary electron from the occupied band. Here we define a binding energy I , which is the amount of energy necessary to reach the Fermi level from an occupied state. Taking this into account, the final energy of the newly ionized electron E_s above Fermi level is then $E_s = \Delta E - I$. The amount of transferred energy ΔE is assumed to be half of the energy of the incident electron ($E/2$) as it was done in [36].

For the inelastic scattering rate (τ_{ee}^{-1}) we will use the energy-dependent collision rate [37] of an excited electron at temperature T_e ,

$$\frac{1}{\tau_{ee}(E, T_e)} = \frac{\pi^2 \sqrt{3}}{128} \frac{\omega_p}{E_f^2} \frac{(\pi k_B T_e)^2 + (E - E_f)^2}{e^{\left(\frac{E - E_f}{k_B T_e}\right)} + 1}, \quad (7)$$

where E_F is the Fermi energy and ω_p is the plasma frequency. For the derivation of equation (7) it is assumed that the band electrons have a Fermi–Dirac distribution.

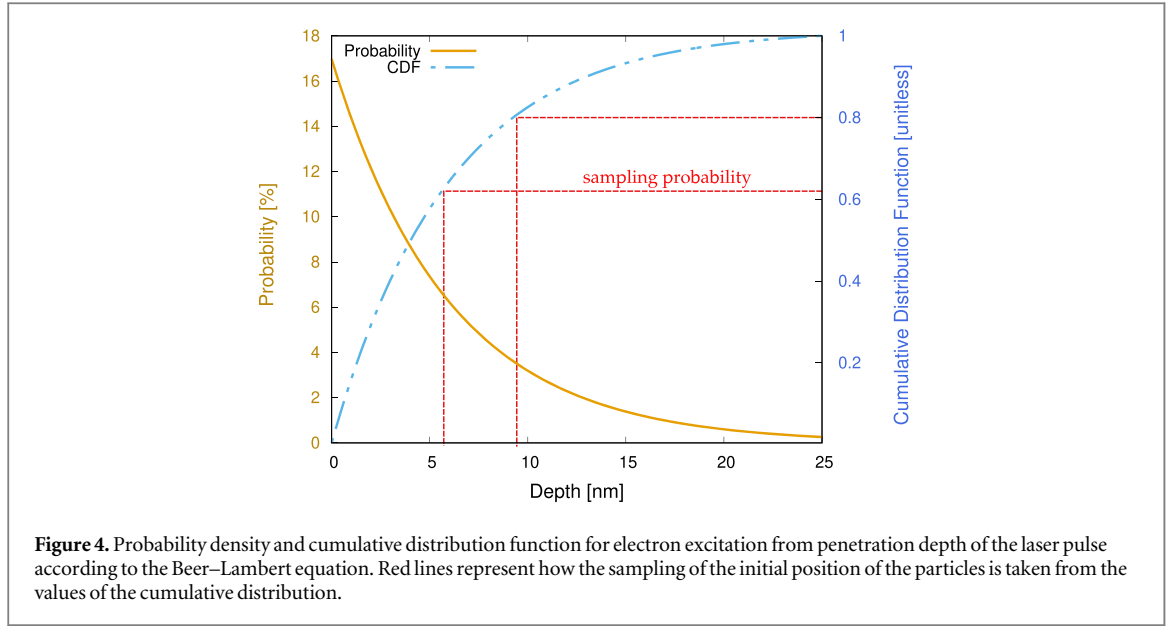


Figure 4. Probability density and cumulative distribution function for electron excitation from penetration depth of the laser pulse according to the Beer–Lambert equation. Red lines represent how the sampling of the initial position of the particles is taken from the values of the cumulative distribution.

For the angle of deflection after an inelastic scattering, we use the classical binary collision model which can be derived from momentum and energy conservation. In collisions between two identical particles with identical masses, the angles of deflection for the primary electron (θ_1) and for the secondary electron (θ_2) are given by

$$\theta_1 = \arcsin\left(\sqrt{\frac{\Delta E}{E_s + \Delta E}}\right), \quad (8)$$

$$\theta_2 = \arcsin\left(\sqrt{\frac{E_s}{\Delta E - I}} \sin \theta_1\right). \quad (9)$$

Since electrons are not distinguishable, we also include a probability that an electron effectively flips its spin. This is an exchange scattering process, due to the Coulomb interaction with electrons in the occupied part of the spin-split band structure, which has been analyzed in terms of the spin-flip self energy by Hong and Mills [38]. While magnons and Stoner excitations can contribute, this scattering processes is called Stoner excitation in [39]. We follow that paper and employ the energy-dependent spin-flip probability in our simulation, see figure 2 in [39].

4. Space dependence

The simulated nonequilibrium system focuses on a one dimensional analysis of the nonequilibrium dynamics along a depth of 25 nm, as sketched in figure 1, but with open boundaries. The absorption profile of the optical excitation imprints a spatial dependence on the initial electron distribution. We take this into account by an excitation probability derived from the Beer–Lambert law. We select the initial position of the excited electrons in the material by randomly sampling the position of excitation from the profile shown in figure 4. The initial direction of movement is sampled randomly as well. The kinetic energies are between Fermi energy E_F and $E_F + 6$ eV, according to the excitation of each individual electron. Then, each electron is traced individually in time and we can monitor its displacement throughout the material.

The motion of electrons can be characterized by the mean square displacement (MSD) [40]. The MSD is defined as the spatial spread of the distribution, which occurs in the transport direction z . As the electrons move, the MSD of their distribution becomes time dependent $\langle(\Delta z)^2\rangle \propto t^\alpha$, where α is known as the generalized diffusion exponent.

The diffusion exponent characterizes the electronic motion under the influence of the excitation and scattering processes. In the ballistic regime, essentially no collisions occur, leading to $\alpha = 2$. Superdiffusive behavior occurs in the intermediate regime with $2 > \alpha > 1$. On longer timescales, the motion of particles is randomized by multiple scattering processes, leading to a diffusive behavior described by $\alpha = 1$.

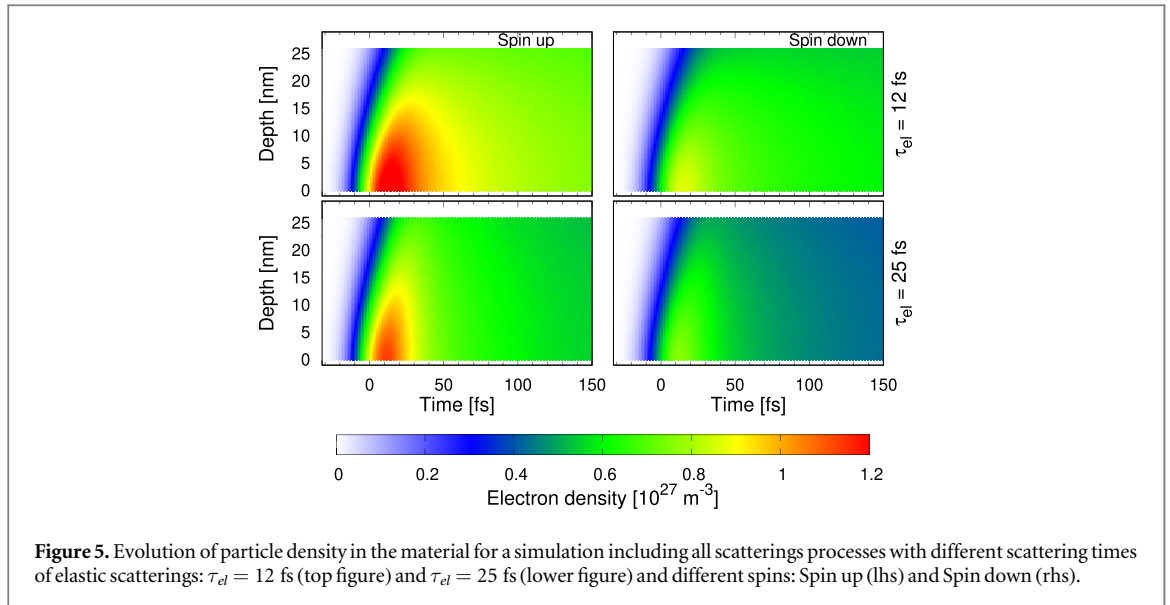


Figure 5. Evolution of particle density in the material for a simulation including all scatterings processes with different scattering times of elastic scatterings: $\tau_{el} = 12$ fs (top figure) and $\tau_{el} = 25$ fs (lower figure) and different spins: Spin up (lhs) and Spin down (rhs).

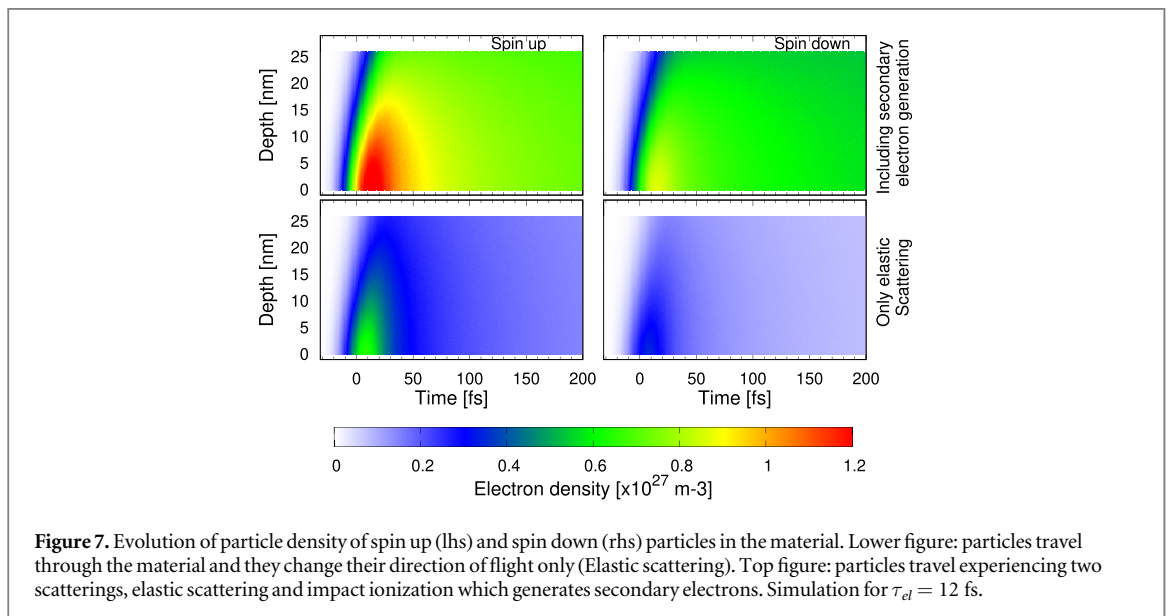
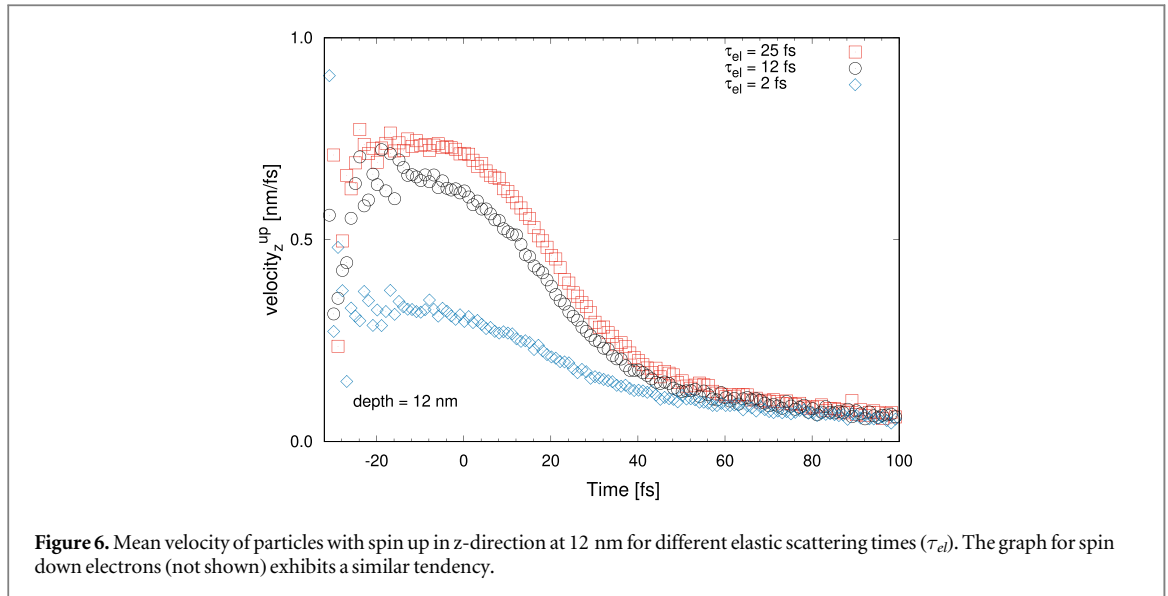
5. Results

The different scattering mechanisms that may occur after fs-laser excitation in ferromagnets affect the nonequilibrium dynamics. The results presented in this work are a consequence of many iterations which are averaged in order to obtain a statistically adequate result. Here we used 10^5 iterations running in parallel through 16 cores and took in average 6 h of computational time. We will focus first on the influence of different scattering rates for elastic scatterings and then discuss the effects of secondary electrons generation. We will analyse the following physical quantities: displacement of the particles, particle velocities, diffusion and spin current.

5.1. Influence of different elastic scattering times

Figure 5 shows the time evolution of the particle density in iron with an open boundary at 25 nm for a simulation where all the scattering processes are included for two different elastic scattering times. The spatio-temporal dynamics of the density of excited electrons is shown in colour code. The surface is at depth zero and the laser is centered at time zero. The upper subplots are for an elastic scattering time of $\tau_{el} = 12$ fs, the lower ones for $\tau_{el} = 25$ fs. One first observes that for the smaller elastic scattering time (upper subplots) the particles remain close to the surface longer. For the smaller elastic scattering time the excited particle density is observable inside the material for larger times. This is because elastic scattering processes occur more often and change the direction of the particles, contributing to the spreading in the material. The red areas in the spin-up channel indicate a higher density of excited spin-up electrons, which is due to the band structure features discussed in the previous section 2 on the photoexcitation process. After about 75 fs the signature of the spatial laser penetration profile has been washed out by scattering processes and transport. The transport characteristics of the dynamics shown here will be analyzed in more detail using the mean square displacement (MSD) in the following subsection.

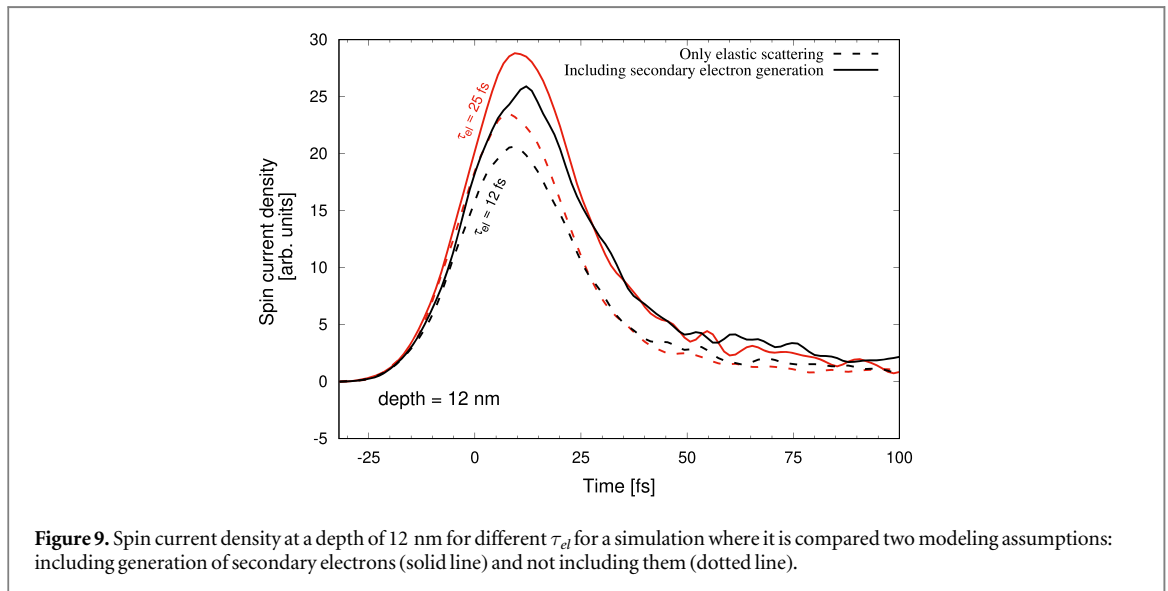
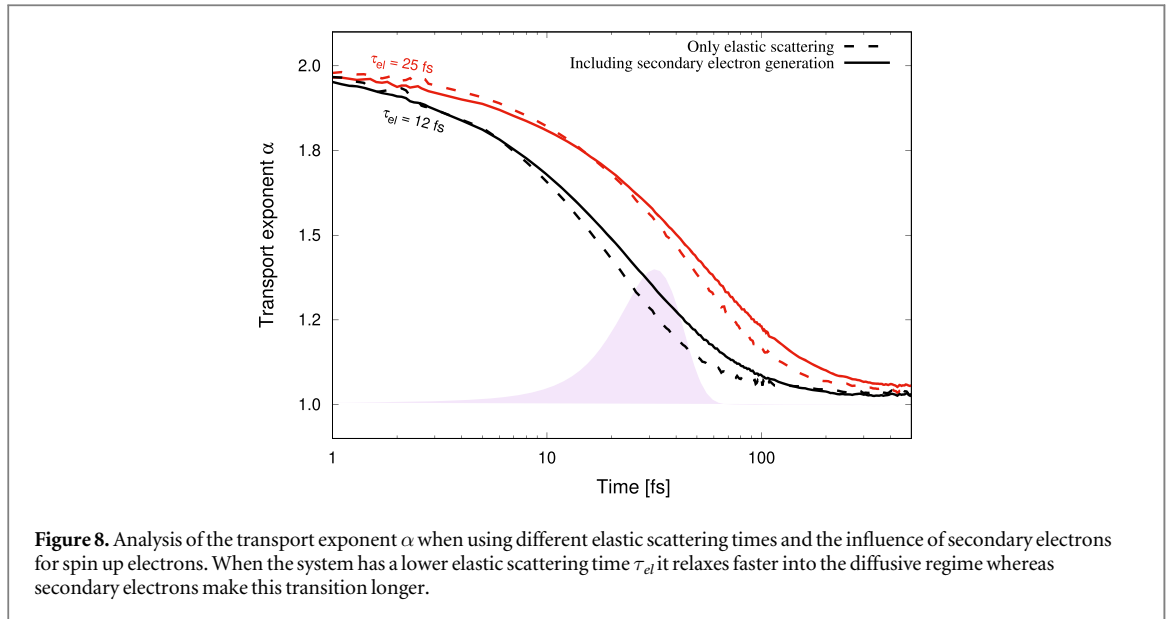
Figure 6 shows the mean velocity in z direction at a depth of 12 nm. Both kinds of spin show only statistical differences, here we show the results for spin up electrons. The mean velocity is calculated as the average velocity in $+z$ direction of all excited particles at the given depth. Apart from the scattering times discussed in section 3.1 we also show results for a third, shorter one ($\tau_{el} = 2$ fs) as a way to study how the system is influenced by lower values of τ_{el} . During the first femtoseconds one can observe higher average velocities with direction into the depth of the material (velocity $_z^{\text{up}} > 0$), but decreasing in magnitude for lower elastic scattering times. In all three cases, the different scattering times keep the velocity of particles on average pointing into the material. After 60 fs the average velocity for all three cases approaches the same value and continues decreasing at the same rate but without reaching zero, which means that a large number of particles travel in $+z$ direction. During the first femtoseconds a smaller magnitude of average velocities towards the depth can be observed for lower elastic scattering time. This is due to a larger number of scatterings that occur influencing the dynamics of electrons traveling through the solid.



5.2. Influence of secondary-electron generation

For the analysis of the influence of secondary electrons (SE) we compare calculations with and without SE. In figure 7 the displacement of particle density in the material for spin up (left hand side) and spin down (right hand side) is presented. The lower subplots shows calculations without including secondary electron generation, labeled ‘only elastic scattering’, whereas the upper subplots show simulations including also impact ionization, labeled ‘including secondary electron generation’ (same as the upper panel of figure 5, repeated here for convenience). During the first femtoseconds, whether secondary electrons are generated or not, one observes a larger concentration of particles near the surface. Later particles spread fast from the surface into the material because more scatterings take place. This indicates that the generation of SEs increases the spread of the particles into the material. The increase in displacement throughout the material can be examined better with the analysis of the motion regimes using the mean square displacement (MSD).

Figure 8 shows a comparison in the evolution of the transport exponent α for two different elastic scattering times τ_{el} with and without the inclusion of secondary electron generation. Only the analysis for spin up electrons is shown because the spin down electrons present on average a similar behavior with only slightly different magnitudes. The data from figures 5 and 7 are analyzed now as described in section 4 using the MSD with the transport exponent α . One can observe for $\tau_{el} = 12$ fs and $\tau_{el} = 25$ fs distinctively all three motion regimes, starting from ballistic, going through superdiffusive and finally becoming diffusive. Since the particles can in principle be initially excited with an arbitrary initial direction pointing into the material, in figure 8 during the first femtoseconds the motion is not entirely ballistic.



The onset of the diffusive regime occurs at different times, it is faster for smaller scattering time. When the secondary electrons come into play, the transition from superdiffusive into diffusive regime is delayed. The generation of secondary electrons effectively increases the duration of electron excitation, influencing the system and keeping it in the superdiffusive regime ($\alpha > 1$) for a longer time in comparison with the other calculations. These results are in agreement with those in [9, 41].

In the study of spin transport, the spin current density j_s is one of the main features to be analyzed. It is defined as

$$j_s(z, t) \propto q[\langle \eta^\uparrow v_\uparrow \rangle - \langle \eta^\downarrow v_\downarrow \rangle], \quad (10)$$

where q is the charge of the electron, η^\uparrow (η^\downarrow) and v_\uparrow (v_\downarrow) are the particle density and the velocity for spin up (spin down), respectively. With this definition the spin current is positive if effectively more spin up electrons move into positive z direction. The spin current density at a fixed depth of 12 nm with (solid line) and without (dashed line) secondary electron generation is shown in figure 9. One can observe that the spin current density changes quantitatively due to the continuous generation of secondary electrons, which feeds excited electrons into the dynamics. Figure 9 shows also a change in the time of maximum intensity in the spin current density when secondary electrons are generated. As a result, the propagation time is longer. In the bulk of the ferromagnet, the spin current does not change sign during the whole simulation. We note that this is different from spin-polarized transport in normal metals where the excitation conditions together with the transport characteristics can lead to a bipolar spin-current signal [9].

6. Summary

In conclusion, we developed a kinetic Monte Carlo method to study the influence of different electron-nucleus collision rates and generation of secondary electrons in the ultrafast nonequilibrium spin and charge transport in Iron. This method simulates kinetics of individual particles based on random sampling, making it a powerful tool for tracing electrons throughout the material. In this simulation we used the probability of excitation according to the material's density of state to excite an electron from an occupied band. Using the displacement and velocity distribution we analyzed the dynamics of excited electrons for different elastic scattering times. We found that lower scattering times increase the average velocity of carriers moving in the material. To assess the influence of secondary electron generation, we focused on its impact in different regimes of motion and for different spin current densities. Generation of secondary electrons effectively delays the excitation of free electrons and thus delays the transition from the ballistic to the diffusive regime. Secondary electrons also affect the intensity of the spin current density and peak. We quantified how the spin dynamics is determined by the elastic scattering time as well as by the generation of secondary electrons which affects experimental observations.

Acknowledgments

Funded by the Deutsche Forschungsgemeinschaft (DFG, German Research Foundation) - TRR 173/2-268565370 Spin+X (Project B03).

Data availability statement

The data that support the findings of this study are available upon reasonable request from the authors.

ORCID iDs

J Briones  <https://orcid.org/0000-0002-9377-6590>

References

- [1] Mueller B Y, Baral A, Vollmar S, Cinchetti M, Aeschlimann M, Schneider H C and Rethfeld B 2013 *Phys. Rev. Lett.* **111** 167204
- [2] Haag M, Illg C and Fähnle M 2014 *Phys. Rev. B* **90** 014417
- [3] Zhang G P and Hübner W 2000 *Phys. Rev. Lett.* **85** 3025–8
- [4] Krieger E, Elliott P, Müller T, Singh N, Dewhurst J K, Gross E K U and Sharma S 2017 *J. Phys. Condens. Matter* **29** 224001
- [5] Steiauf D and Fähnle M 2009 *Phys. Rev. B* **79** 140401
- [6] Battiato M, Carva K and Oppeneer P M 2010 *Phys. Rev. Lett.* **105** 027203
- [7] Rudolf D et al 2012 *Nat. Commun.* **3** 1037
- [8] Berggaard N, Hehn M, Mangin S, Lengaigne G, Montaigne F, Laliu M L M, Koopmans B and Malinowski G 2016 *Phys. Rev. Lett.* **117** 147203
- [9] Nenno D M, Rethfeld B and Schneider H C 2018 *Phys. Rev. B* **98** 224416
- [10] Nikjoo H, Uehara S, Emfietzoglou D and Brahme A 2008 *New J. Phys.* **10** 075006
- [11] Medvedev N and Rethfeld B 2009 *EPL (Europhysics Letters)* **88** 55001
- [12] Huthmacher K, Herzwurm A, Gnewuch M, Ritter K and Rethfeld B 2015 *Physica A* **429** 242–51
- [13] Morales M, Guimarães C C, Bonifácio D A B, Okuno E, Murata H M, Bottaro M, Menezes M O and Guimarães V 2009 Applications of the Monte Carlo method in nuclear physics using the GEANT4 toolkit *AIP Conf. Proc.* **1139** 51–6
- [14] Zimmerman G B and Adams M L 1991 Algorithms for Monte Carlo particle transport in binary statistical mixtures 1991 *Winter meeting of the American Nuclear Society (ANS) session on fundamentals of fusion reactor thermal hydraulics* 63 (<https://www.osti.gov/biblio/7011618>)
- [15] Eckstein W 1991 *Computer Simulation of Ion-Solid Interactions* 1st edn (Berlin: Springer) (<https://doi.org/10.1007/978-3-642-73513-4>)
- [16] Haghight A 2014 *Monte Carlo Methods for Particle Transport* (Boca Raton: CRC Press)
- [17] Spin dependent density of states for iron (<http://lampx.tugraz.at/hadley/ss1/materials/dos/iron.html>)
- [18] Kallenberg O 2002 *Foundations of Modern Probability* 3rd edn (Berlin: Springer) (<https://doi.org/10.1007/978-3-030-61871-1>)
- [19] Carl Graham D T 2013 *Stochastic Simulation and Monte Carlo Methods* 1st edn (Berlin: Springer) (<https://doi.org/10.1007/978-3-642-39363-1>)
- [20] Rees H 1968 *Phys. Lett. A* **26** 416–7
- [21] Czyżewski Z, MacCallum D O, Romig A and Joy D C 1990 *J. Appl. Phys.* **68** 3066–72
- [22] Gombás P 1949 *Die Statistische Theorie des Atoms und ihre Anwendungen* 1st edn (Berlin: Springer) (<https://doi.org/10.1007/978-3-7091-2100-9>)
- [23] Jablonski A, Salvat F and Powell C J 2004 *J. Phys. Chem. Ref. Data* **33** 409–51
- [24] Dapor M 1995 *Nucl. Instrum. Methods Phys. Res., Sect. B* **95** 470–6
- [25] Lin Z, Zhigilei L V and Celli V 2008 *Phys. Rev. B* **77** 075133
- [26] Medvedev N and Milov I 2020 *Phys. Rev. B* **102** 064302

- [27] Chen J K, Latham W P and Beraun J E 2005 *J. Laser Appl.* **17** 63–8
- [28] Lee J B, Kang K and Lee S H 2011 *Materials Transactions* **52** 547–53
- [29] Kruglyak V V, Hicken R J, Ali M, Hickey B J, Pym A T G and Tanner B K 2005 *Phys. Rev. B* **71** 233104
- [30] Kaltenborn S, Zhu Y H and Schneider H C 2012 *Phys. Rev. B* **85** 235101
- [31] Wilson R B and Coh S 2020 *Communications Physics* **3** 2399–3650
- [32] Bezhnov S and Uryupin S 2022 *Int. J. Heat Mass Transfer* **184** 122308
- [33] Eschenlohr A, Battiato M, Maldonado P, Pontius N, Kachel T, Holldack K, Mitzner R, Föhlisch A, Oppeneer P M and Stamm C 2013 *Nat. Mater.* **12** 332–336
- [34] Gryziński M 1965 *Phys. Rev.* **138** A336–58
- [35] Wolff P A 1954 *Phys. Rev.* **95** 56–66
- [36] Ritchie R and Ashley J 1965 *J. Phys. Chem. Solids* **26** 1689–94
- [37] Mueller B Y and Rethfeld B 2013 *Phys. Rev. B* **87** 035139
- [38] Hong J and Mills D L 2000 *Phys. Rev. B* **62** 5589–600
- [39] Mao S F, Sun X, Fang X W, Da B and Ding Z J 2012 *Surf. Interface Anal.* **44** 703–8
- [40] Michalet X 2010 *Phys. Rev. E* **82** 041914
- [41] Battiato M, Carva K and Oppeneer P M 2012 *Phys. Rev. B* **86** 024404